Integrating Materials and Manufacturing Innovation (2023) 12:105–117
https://doi.org/10.1007/s40192-023-00294-7

TECHNICAL ARTICLE

Computational Efficient Modeling of Supersolidus Liquid Phase Sintering in Multi-component Alloys for ICME Applications

Tesfaye T. Molla[1]

Received: 8 November 2022 / Accepted: 1 March 2023 / Published online: 16 March 2023

Abstract

One of the challenges in computational design of pre-alloyed powders for sintering is the absence of predictive, efficient, and fast acting models that enable the design space of alloys to be tractable. This study presents an efficient and predictive model to simulate the densification as well as shape distortion of pre-alloyed powder compacts during supersolidus liquid phase sintering (SLPS). The model combines the generalized viscous theory of sintering with microstructural models for diffusional creep accommodated by viscous grain boundary sliding. Critical model parameters are obtained from thermodynamic modeling based on the calculation of phase diagrams (CalPhaD) and simulations of diffusional transformations in metals. The model is validated by comparing simulation results with experimental data from the literature for various types of engineering alloys. In addition, a processing window for defect free sintering of samples is presented by defining a microstructural softening parameter for a sintering body. The model can be used in the design of pre-alloyed powders for SLPS within the context of an integrated computational materials engineering (ICME) frameworks.

Keywords Supersolidus liquid phase sintering (SLPS) · Sintering · Integrated computational materials engineering (ICME) · Alloy design

Introduction

Computational material design is a top–down, model/simulation assisted decision-making process aiming to determine the materials composition and/or processing parameters necessary to meet performance requirements [1, 2]. The design and development of multi-component alloys can be guided by a set of functional properties required of the component or artefact (e.g., strength, hardness, etc.). In some cases, the design of alloys should also be guided by the requirement for efficient processing or manufacturing as much as for property. An example is the design of pre-alloyed powders for manufacturing of components via powder metallurgy (PM) route where a special heat treatment step (sintering) is critical to turn the porous powder compact (green body) into a usable solid [3].

Computational design of pre-alloyed powders for efficient sintering requires simulating the alloy's behavior under a given sintering cycle. This requires not only reliable but also predictive models that are able to capture the effect of, for instance, compositional variations on the sintering performance of the alloy. Complex numerical models (e.g., physically based multi-scale models) are often used to study the behavior (i.e., densification as well as shape evolution) of porous compacts during sintering. However, the use of these models for computational design of materials is currently unrealistic because of the computational cost associated with exploring the multi-dimensional design space of alloys. For example, an alloy with seven components where the concentration of each component can take ten values may require at least 10^7 individual simulations over a given sintering cycle during computational exploration to identify the optimal alloy [4]. Efficient and fast acting models that can simulate the sintering response of pre-alloyed powders are thus critical for computational design of particulate materials.

We have previously demonstrated an efficient model for simulating the sintering response of pre-alloyed powders during solid state sintering for ICME (integrated computational materials engineering) applications [5]. The present work builds on that to address special case of sintering commonly referred to as supersolidus liquid phase sintering

✉ Tesfaye T. Molla
tesfaye.molla@unimelb.edu.au

[1] Department of Mechanical Engineering, The University of Melbourne, Parkville, VIC 3010, Australia

(SLPS). SLPS is often used to enhance densification of pre-alloyed powder compacts [6]. During SLPS, pre-alloyed powders are heated to a temperature between the solidus and liquidus [6]. The liquid phase forms within each particle and spreads along the grain boundaries resulting in fragmentation of the powder particles. The capillary force generated by the liquid meniscus between the powders drives viscous grain boundary sliding and hence densification through re-arrangement of grains. Densification occurs rapidly when there is enough liquid to fragment the powders into individual grains, making SLPS effective even for samples with relatively coarse powder particles [6, 7].

Modeling the SLPS of pre-alloyed powders is essential to control the sintering process, including the densification and macrostructural shape evolution. It has been shown that the sintering body during SLPS, involving fragmented particles with a liquid phase, deforms in a viscous manner [6, 8, 9]. Thus, the macroscopic deformation of the sintering body is often described by viscous material models, which requires knowledge of the viscous properties of the powder compact at high temperatures. Previously reported works on modeling the behavior of pre-alloyed powders during SLPS [6, 8–12] relied either on experimental characterization to obtain the viscous properties of the powder compact or on the use of over-simplified assumptions. These limitations in the predictive capability of the models make them less attractive for computational design applications.

In this work, a computational efficient model for simulating the sintering behavior of pre-alloyed powders during SLPS without the need for characterizing the viscous properties of powder compacts is suggested. The model is developed by combining the generalized viscous theory of sintering together with microstructural models for diffusional creep accommodated by viscous grain boundary sliding and rotation. Implementation of the model includes computational thermodynamic modeling based on the calculation of phase diagrams (CalPhaD) and simulations of diffusional transformations in metals to evaluate the viscous properties of the powders at sintering temperatures. The predictive capability of the model is validated by comparing simulation results with experimental data from the literature for densification and shape distortion during SLPS of powder compacts for a variety of engineering alloys.

Model for Densification and Shape

The Constitutive Model

In the continuum solid mechanics framework, deformation in porous compacts at the sintering temperature is rate dependent where the total strain rate tensor, $\dot{\varepsilon}_{ij}^{\text{tot}}$ is given by considering the elastic, $\dot{\varepsilon}_{ij}^{\text{el}}$, thermal, $\dot{\varepsilon}_{ij}^{\text{th}}$, and sintering, $\dot{\varepsilon}_{ij}$ components as [13]:

$$\dot{\varepsilon}_{ij}^{\text{tot}} = \dot{\varepsilon}_{ij}^{\text{el}} + \dot{\varepsilon}_{ij}^{\text{th}}\delta_{ij} + \dot{\varepsilon}_{ij} \tag{1}$$

where the dot denotes the time derivative and δ_{ij} is Kronecker delta (i.e., $\delta_{ij}=1$ if $i=j$ and $\delta_{ij}=0$ if $i\neq j$). The elastic strain during sintering is negligible [14] and the thermal strains are magnitudes smaller than the sintering strains. Thus, the deformation in the sintering body can be approximated by considering the sintering strain rate only.

Shrinkage in pre-alloyed powder compacts during SLPS is controlled by the relative sliding rate of grains over each other, resulting in re-arrangement of the grains in response to the capillary stress [6, 8, 9]. In addition, the macroscopic shape distortion is due to the shear deformation of the semi-solid powder compact, which exhibits pseudoplastic or viscous behavior at high temperatures. Thus, if the viscous constitutive parameters of the powder compact are known, the macroscopic sintering strain rate during SLPS of multi-component alloys can be modeled using the generalized viscous theory of sintering. Accordingly, the inelastic strain rate, $\dot{\varepsilon}_{ij}$ of the sintering body is given by [15]:

$$\dot{\varepsilon}_{ij} = \frac{\sigma'_{ij}}{\eta_o \varphi} + \frac{\sigma_{\text{m}} - \sigma_{\text{s}}}{3\eta_o \psi}\delta_{ij} \tag{2}$$

where σ_{ij}', σ_{m} and σ_{s} refer to the shear, mean and the effective sintering stresses, respectively. η_o represents the shear viscosity of the semi-solid sintering body, which varies with temperature, grain size and the volume fraction of the liquid phase. It is in general given by a "power-law" equation as [6, 16]:

$$\eta_o = K\dot{\gamma}^{n-1} \tag{3}$$

where K is a constant, $\dot{\gamma}$ is the equivalent shear rate, and n is the power-law index. The power-law index determines whether the viscous deformation in the sintering body is linear or non-linear [15].

The first term in the right-hand side of Eq. (2) represents the shear strain rate, $\dot{\varepsilon}'_{ij}$ which leads to shape loss of the sintering body. The second term refers to the linear component of the volumetric shrinkage rate, i.e., $\dot{\varepsilon}_{ij}\delta_{ij}$. According to the viscous theory of sintering, the φ and ψ terms in Eq. (2) refer to the normalized shear and bulk viscosities, usually defined by using the fraction of instantaneous porosity, θ in the sintering body as [15]:

$$\varphi = (1-\theta)^2; \psi = \frac{2}{3}\frac{(1-\theta)^3}{\theta} \tag{4}$$

The re-arrangement of grains and/or particles during SLPS is driven by a capillary stress (sintering stress), which

is generated by the intrinsic tendency of the material to minimize the total interfacial energy of the system. Since the overall powder compact behaves in a viscous manner, the effective sintering stress, σ_s is given by the product of the local sintering stress,$\sigma_{so} = 4\gamma_{lv}/d_p$ and the normalized sintering stress, $\overline{\sigma}_s = \frac{1}{2}(1-\theta)^2$ as [6, 15]:

$$\sigma_s = \frac{2\gamma_{lv}}{d_p}(1-\theta)^2 \tag{5}$$

Here, γ_{lv} is the surface energy per unit area of the liquid meniscus at the particle neck and d_p is the instantaneous mean diameter of the pores [6, 15, 17]. The mean pore diameter at the on-set of sintering can be found by using the mean size of the powder particles, D_p and porosity, θ as [6]:

$$d_p = D_p\left(\frac{\theta}{1-\theta}\right)^{1/3} \tag{6}$$

The time evolution of the relative porosity (or density) can thus be evaluated using the continuity equation for viscous bodies, which relates the volumetric shrinkage, $\dot{\varepsilon}_{kk} = \sum \dot{\varepsilon}_{ij}\delta_{ij}$ with the rate of evolution of fractional porosity, $\dot{\theta}$ as [15]:

$$\dot{\varepsilon}_{kk} = \frac{\dot{\theta}}{1-\theta} \tag{7}$$

Provided that all the necessary parameters (i.e., material, process, and geometric parameters) are known, this model can be used to integrate the relative density, i.e., $\rho = (1-\theta)$ and deformation in the form of linear strain at any point across the sample geometry.

Kinetics of Shrinkage and Shape Loss in Cylindrical Samples

Figure 1 shows schematics of a cylindrical sample and the microstructure of the powder compact during SLPS. Shape loss or distortion can be caused by the weight of the sample, which can generate a net deviatoric component of stress, σ_{ij}'

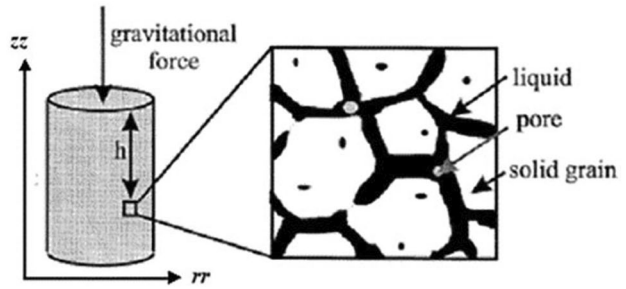

Fig. 1 Schematic of cylindrical sample and the microstructure toward the end of SLPS [7]

in the direction of the gravitational force. Usually, the effect of gravity is negligible during the initial and intermediate stages of sintering because the sintering stress (which is proportional to the pore fraction) is significantly greater than the gravitational force. However, as densification proceeds and the pore fraction decreases, the effect of gravity becomes pronounced, causing the sample to slump or distort.

By using a spherical coordinate system, the shear stress due to weight at a given point is directed vertically (-*zz* direction), see Fig. 1, and is constant throughout the sintering cycle. The deviatoric and mean components of the stress due to weight of the cylindrical sample can be given, respectively, by:

$$\sigma_{zz}' = \tfrac{2}{3}\rho_b g h;\ \sigma_m = \tfrac{1}{3}\rho_b g h \tag{8}$$

where ρ_b is the instantaneous density, which can be calculated from the relative and theoretical densities as: $\rho_b = \rho_x\rho_t$; g is the acceleration due to gravity and h is the height measured from the top surface of the sample.

Gravity induces spatial differences in the shrinkage rate across the sample geometry. For example, there is zero gravitational effect at the top of the sample and hence the shrinkage rate is driven entirely by the intrinsic sintering stress. On the other hand, the shrinkage rate at the bottom of the sample is affected by the gravitational force proportional to the height of the sample. Therefore, by combining Eq. (2) and (8), it is possible to estimate the total vertical shrinkage rate, at the top, $\dot{\varepsilon}_{zz}^t$, and bottom, $\dot{\varepsilon}_{zz}^b$, of the sample, respectively, as:

$$\dot{\varepsilon}_{zz}^t = \frac{-\sigma_s}{3\eta_o\psi};\ \dot{\varepsilon}_{zz}^b = \frac{\frac{2}{3}\rho_b g h}{\eta_o\varphi} + \frac{\sigma_m - \sigma_s}{3\eta_o\psi} \tag{9}$$

Assuming no friction between the sample and surface of the sintering furnace, the radial strain rate at the bottom of the sample, $\dot{\varepsilon}_{rr}^b$, can be estimated by considering the viscous Poisson's ratio, v [18] as:

$$\dot{\varepsilon}_{rr}^b = -v\left(\frac{\frac{2}{3}\rho_b g h}{\eta_o\varphi}\right) + \frac{\sigma_m - \sigma_s}{3\eta_o\psi} \tag{10}$$

The corresponding relative density or porosity evolution at the bottom of the cylindrical sample can also be estimated using Eq. (7) and considering the strain rates in all directions as:

$$\dot{\theta} = \left(\dot{\varepsilon}_{rr}^b + \dot{\varepsilon}_{zz}^b + \dot{\varepsilon}_{\theta\theta}^b\right)(1-\theta) \tag{11}$$

Note that the strain rate in the angular direction, $\dot{\varepsilon}_{\theta\theta}^b$ is not affected by gravity and hence it can be assumed equal to the strain rate at the top of the sample (free strain rate). The magnitude of the distortion or shape loss can be calculated by integrating the radial shrinkage rates across the height of a cylindrical sample over the sintering time.

Obtaining the Viscous Constitutive Parameter

In this section, we propose a model to evaluate the shear viscosity of the sintering body, η_o so that the model discussed in "The Constitutive Model" section can be used to simulate the SLPS of samples (shrinkage as well as shape losses) without the need for additional characterization experiments.

The viscosity that controls deformation of the powder compact during SLPS should be determined by considering the mechanisms by which deformation occurs. For example, if densification is dominated by solution reprecipitation, then there will be solid dissolution into the liquid, diffusion of the solute in the liquid and finally precipitation of the dissolved solid on larger grains. In this case, diffusion of the solute elements in the liquid medium defines the deformational behavior (viscosity) of the powder compact.

However, during SLPS, the sintering body becomes soft or semi-solid due to the liquid phase between the grains. Figure 2 shows schematics of the microstructure of a powder compact with liquid phase distributed between grains. This implies that the deformation through diffusional creep is accommodated by viscous grain boundary sliding and grain rotation. Both diffusion and grain boundary sliding contribute to the deformation and hence re-arrangement of the particles. The diffusivity of the solute through the solid and liquid medium is not the only factor that determines the viscosity of the powder compact. The sliding rate of grains is also critical to re-arrangement. Therefore, the model for viscosity of the sintering body needs to incorporate the effects of grain boundary sliding as well as diffusion.

Kim et al.[19] developed a model for sliding of viscous grain boundary in polycrystalline materials during diffusional creep at high temperatures. Here, we extend Kim et al.*'s* model for the relative sliding rate, v_s, of hexagonal grain boundary interfaces to strain rate during SLPS. The shear strain rate between grains can be given by $\dot{\varepsilon}'_{ij} = v_s/d$, which can further be written using a macroscopic shear stress, $\sigma_{ij}{}'$ as:

$$\dot{\varepsilon}'_{ij} = \frac{CD_s\delta_L\Omega}{d^3kT}\sigma'_{ij}\left[\frac{2}{9}+\frac{5}{6}\tilde{\eta}\right]^{-1} \tag{12}$$

where C is a constant, D_s is the self-diffusion coefficient of the base metal in the alloy, δ_L is the mean film thickness, Ω is the atomic volume, k is the Boltzmann constant, d is mean grain size, T is temperature in Kelvin, $\tilde{\eta}_l$ is the normalized viscosity for grain boundary sliding, which is given by $\eta_l\Omega D_s/d^2kT$ where η_l is viscosity of the liquid phase between the grain boundaries.

Combining the shear strain component of Eq. (2) with Eq. (12), a relation for the temperature-dependent shear viscosity, η_o of the semi-solid sintering body can be found as:

$$\eta_o = \frac{d^3kT}{D_s\delta_L\Omega\varphi}\left[\frac{2}{9}+\frac{5}{6}\tilde{\eta}\right] \tag{13}$$

Equation (13) shows that the shear viscosity of the semi-solid body increases with a decrease in the liquid film thickness. The mean liquid film thickness between the grain boundaries, δ_L, depends on the grain size, d, the volume fraction of the liquid at the sintering temperature, f_l, and the fractional coverage of grain boundaries by the liquid, F_c as [7]:

$$\delta_L = \frac{df_l}{3F_c(1-f_l)} \tag{14}$$

There is also a unique fractional coverage of the grain boundaries, F_c for a given dihedral angle and liquid content, which is given by $F_c = 2.64(f_l/\alpha)^{\frac{2}{3}}$ where α is a function of the dihedral angle as given by [7].

Thermodynamic Modeling

Implementation of the model discussed in "Obtaining the Viscous Constitutive Parameter" section requires material parameters including the self-diffusion coefficient and volume fraction of liquid phase at the sintering temperature. These parameters are calculated using thermodynamic

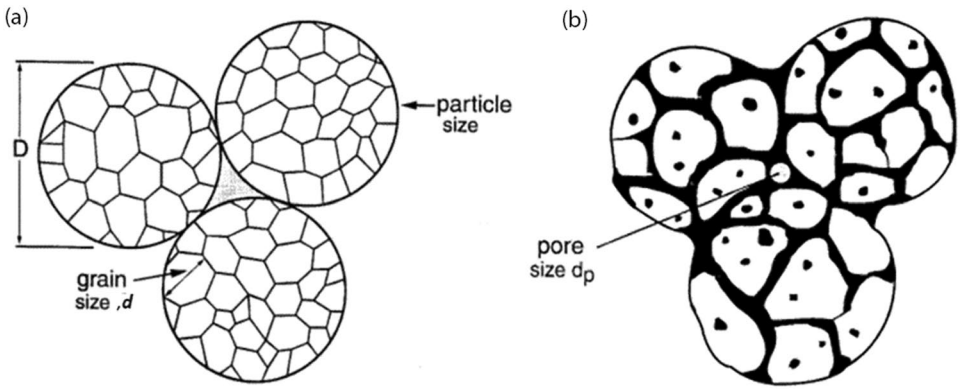

Fig. 2 Schematics of microstructure of a powder compact at the **a** initial and **b** final stages of SLPS, adapted from [6]

simulations of the multi-component alloys, which enables all the composition and microstructural phases at the sintering temperatures to be considered. This is achieved by using Thermo-Calc, a CalPhaD (calculation of phase diagram) based thermodynamic simulation software package, coupled with the simulation of diffusional transformation in metals (DICTRA).

The thermodynamic computations are performed by coupling CalPhaD and DICTRA with the thermodynamic and mobility databases for iron (Fe) and aluminum (Al)—based alloys, namely TCFE9, TCAL, MOBFE4 and MOBAL4, respectively. Details of the method are explained in Molla et al.[5]. In addition, the viscosity of the liquid phase at the sintering temperature is determined using the property calculation module available in Thermo-Calc (TC), which also makes use of thermodynamic and mobility databases.

Model Validation and Discussion

Material Systems and Determination of Input Parameters

To demonstrate the capability of the model discussed in "Model for densification and shape" section, experimental data from the literature [20–23] for the sintering behavior of three groups of material systems are considered, including (i) high-speed steels (HSS), (ii) stainless steels (SS) and (iii) aluminum alloys (AA). Compositions of the alloys in each group, together with the names used in the corresponding references, are summarized Table 1. The experimental data includes densifications for all and shape loss for some of these alloys at various temperatures.

Wright et al. [20] investigated the sensitivity of the sintering behavior of high-speed steel alloys to variations in carbon composition and sintering temperature. Bollina [21] studied the supersolidus liquid phase sintering of gas and water atomized stainless steels (GA316L and WA316L) after examining changes in the densification behavior due to the addition of 0.2 and 0.8 wt% of elemental boron (B) in each alloy. In addition, Lui et al. [22] and Momeni et al. [23] showed the effect of adding various amounts of tin (Sn) on the densification behavior of aluminum alloys 6061 and 2024, respectively.

The material systems in Table 1 are chosen in a way to demonstrate the capability of the model suggested in this study. Note that the observed changes in the sintering behaviors in each group of the alloys provided in Table 1 are mainly associated with the changes in the material (chemical) composition. By predicting the observed material related changes during sintering, it is possible to validate the model and show its usefulness in the computational design of pre-alloyed powders for supersolidus liquid phase sintering.

Critical input parameters for the model, particularly the volume fraction of liquid phase and the self-diffusion coefficient of each alloy as a function of the sintering temperatures are determined using thermodynamic calculations as per the discussion in "Thermodynamic Modeling" section. Figure 3a–f shows the liquid volume fraction and the self-diffusion coefficients as a function of temperature for each of the alloys in Table 1, calculated using Thermo-Calc. Note that the calculations are performed for the temperature ranges over which the sintering behavior is reported.

As shown in Fig. 3, the addition of 0.1 wt% carbon to high-speed steel reduces the solidus temperature, increasing the diffusivity at lower temperatures. Similarly, the addition

Table 1 Chemical composition of selected alloys in wt%

High-speed steels (HSS) [20]							
	Fe	C	Cr	Mo	V	Co	O
P2A	Bal	1.25	–	12.7	–	–	0.14
P2B	Bal	1.35	–	12.7	–	–	0.14
P2C	Bal	1.45	–	12.7	–	–	0.14
Stainless steel (SS) [21]							
	Fe	Cr	Ni	Mo	Mn	Si	P
GA316L	Bal	16.9	11.7	2.3	1.80	0.10	0.05
WA316L	Bal	16.3	13.4	2.2	0.21	0.10	0.05
Aluminum alloys (AA) [22, 23]							
	Al	Mg	Si	Cu	Fe	Cr	Mn
6061	Bal	0.95	0.65	0.27	0.13	0.15	–
2024	Bal	1.23	0.45	3.95	0.27	–	0.36

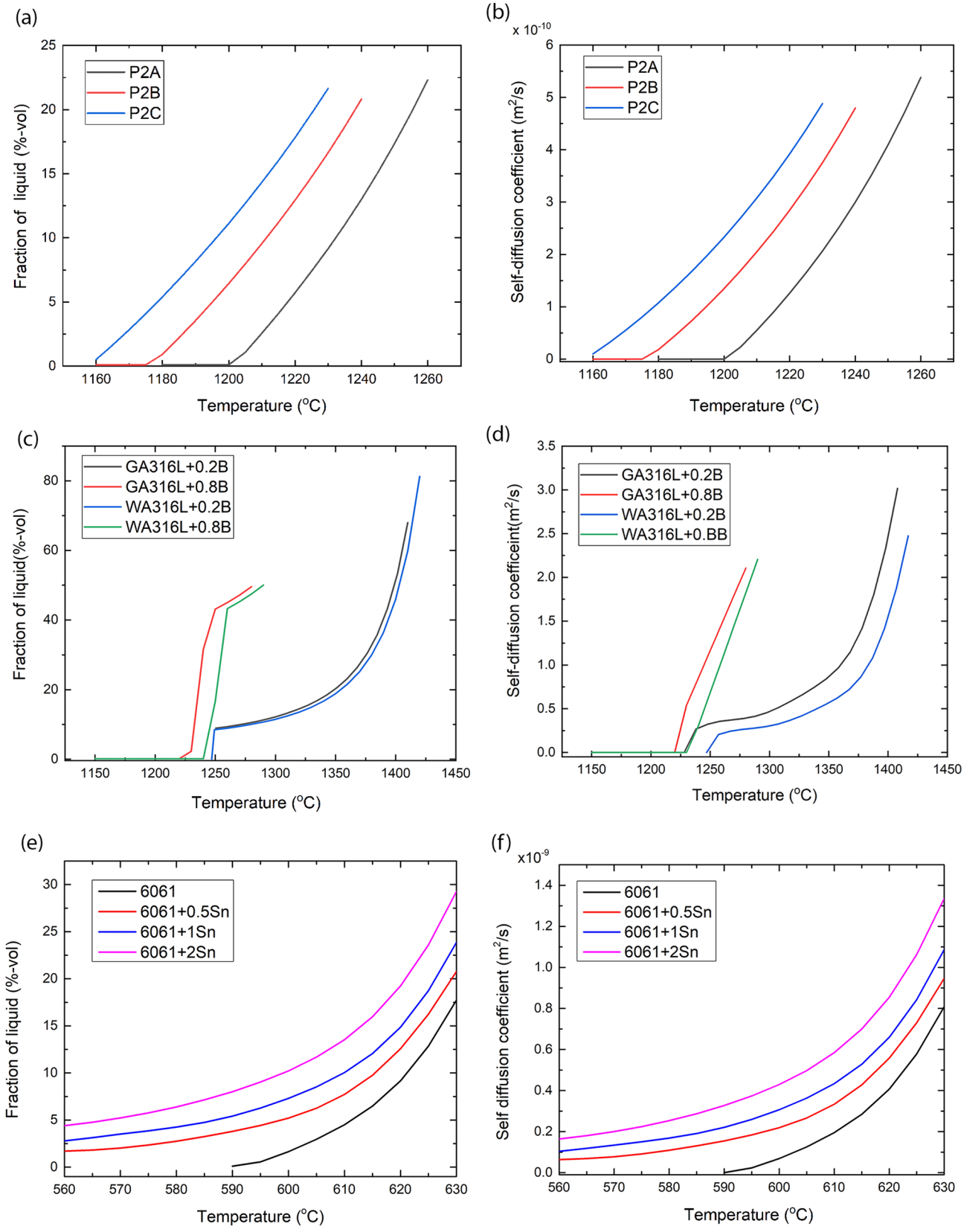

Fig. 3 Material parameters as calculated using Thermo-Calc for the three groups of alloys provided in Table 1. **a**, **c** and **e** show the volume fraction of liquid versus temperature; **b**, **d** and **f** show the self-diffusion coefficient versus temperature. High-speed steels are shown in (**a**) and (**b**); stainless steels in (**c**) and (**d**); and aluminum in (**e**) and (**f**)

of boron to gas and water atomized stainless steel changes the solidus temperature and increases the change in fraction of the liquid phase with respect to temperature. This is consistent with the experimental results reported by Bollina [21]. On the other hand, the addition of Sn to Al-alloys reduces the solidus temperature significantly, making sintering at lower temperature possible. In general, the observed change in the volume fraction of the liquid is followed by a similar change in the self-diffusion coefficient of the alloys. This is consistent with the expectation that diffusivity will be enhanced with the formation of a liquid phase.

Other model parameters, which are related to the atomic properties, are considered based on the characteristics of the base element in each alloy. Summary of these parameters for the three groups of alloys are shown in Table 2. Note that the slight variation of surface energy with temperature during the sintering cycles is assumed to be insignificant and hence a constant value is considered. This is consistent with previous studies involving modeling of the sintering process [6, 24].

To reproduce the observed sintering behavior of the alloys provided in Table 1, it is also important to consider the processing parameters used during the experiments. These parameters are collected from the experimental procedures described in the corresponding literature and summarized in Table 3 for the three groups of alloys considered in this study.

Note that the model in this study is implemented by approximating the powder compacts as if they are made from a homogenous distribution of spherical powders. Thus, the initial powder size in each case is represented by the reported mean values. This approximation will obviously compromise the absolute accuracy of the model but makes it fast acting and useful for computational design of materials by efficiently exploring the relative response of thousands of alloy systems to a sintering profile.

The other important factor that affects the viscosity of the powder compact and hence the sintering rate is coarsening of grains, see Eq. (13). In this study, coarsening of grains is considered by using a model for grain growth kinetics. Accordingly, the mean grain size, d during SLPS is estimated by using a grain growth coefficient k_g together with an apparent activation energy for grain growth, E_g and gas constant, R for a given initial mean grain size, d_o, sintering temperature, T and time, t as [18]:

$$d^3 = d_o^3 + k_g \exp\left(-\frac{E_g}{RT}\right)t \tag{15}$$

If the initial and final grain sizes are known for a given sintering temperature and time, the grain growth coefficient, k_g and apparent activation energy, E_g can be determined. This can be done by starting the grain growth simulation with realistic guesses of the two unknown parameters, i.e., k_g and E_g in the grain growth model. The unknown parameters can then be identified as those providing the minimum deviation as per Eq. (16) between the model simulation, d^{sim} and experimental data, d^{exp}. Here, the sum can be taken over N data points. A similar methodology has been used successfully by Molla et al. [18] to estimate the viscous parameters of a sintering body during solid state sintering.

$$\Delta = \left[\sum_{i=1}^{N}\left(\frac{d^{sim} - d^{exp}}{\text{mean}(d^{exp})}\right)^2\right]^{\frac{1}{2}} \tag{16}$$

Thus, by using the mean grain size data reported by Bollina [21], the apparent activation energies, E_g, during SLPS for boron doped gas and water atomized stainless steels are determined to be 340 kJ/mol and 1300 kJ/mol, respectively. These results are consistent with the values reported by Bollina [21, 26], where the high activation energy for boron doped water atomized stainless steel is explained by

Table 2 Model parameters used to calculate sintering performance

Parameters	HSS [25]	SS [25]	AA [25]
Atomic volume, Ω [m^3]	1.13×10^{-29}	1.13×10^{-29}	1.16×10^{-29}
Surface energy of solid, γ_{sv} [J/m^2]	1.50	1.50	0.90
Surface energy of liquid, γ_{lv} [J/m^2]	1.00	1.00	0.85
Boltzmann constant, k [J/K]	1.38×10^{-23}	1.38×10^{-23}	1.38×10^{-23}
Gas constant, R [J/mol.K]	8.31	8.31	8.31

Table 3 Processing parameters for alloys provided in Table 1

Parameters	HSS [20]	SS [21, 26]		AA [22, 23]	
		GA316L	WA316L	AA6061	AA2024
Sintering temperature, T [°C]	1150–1270	1150–1440	1150–1440	560–630	570–620
Sintering time, t [hrs]	1.0	0.5	0.5	2.0	0.5
Mean initial particle size, R [μm]	100	10	48	13.4	75
Initial mean grain size, d_o [μm]	1.0	1.0	48	1.3	7.5
Green densities, ρ_o [%]	72.5	73	73	50	67.5
Sample height, h [mm]	5	15	15	2.5	10

pore pinning [26]. Similarly, by using the mean grain size data reported by Momeni et al. [23], the apparent activation energy for aluminum alloys is estimated to be 320 kJ/mol. In the case of high-speed steels, the final grain sizes at different sintering temperatures are estimated from the microstructures in [20], which are then used with Eq. (16) to extract the primary phase grain growth parameters. Note that the grain growth coefficient, k_g is largely independent of the initial grain sizes [27] and hence the approach adopted here can be used to estimate the grain growth parameters, which are necessary to incorporate coarsening of grains into the proposed sintering model.

Validation of Densification

By using the material and process parameters identified in "Material Systems and Determination of Input Parameters" section, the model discussed in "Model for densification and shape" section is integrated over the sintering duration to estimate the relative density after sintering at different temperatures. The experimental measurements for the three groups of alloys and the results of the simulations are shown in Figs. 4, 5, and 6. The model predictions agree with the measurements. Particularly, the models are able to clearly show the difference in the densification behavior due to variations in composition (in some cases, due to the addition of a very small amount of elemental powders).

In the case of high-speed steels, densification before the formation of liquid in the microstructure (i.e., below the solidus temperature) is very small, and it increases rapidly with an increase in the liquid fraction. This is demonstrated both in the experimental measurements and model predictions.

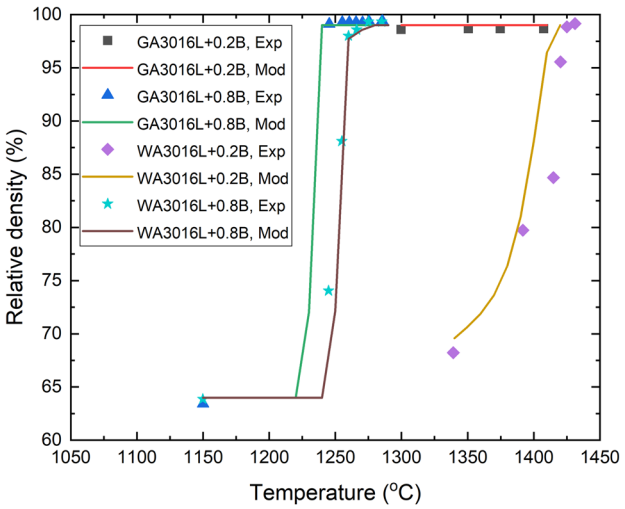

Fig. 5 Comparison of model and experimental measurements [21] for sintered densities as a function of temperature in four stainless steels

However, the solidus temperatures from the experiment (1190, 1168, and 1153 °C for P2A, P2B and P2C, respectively) differ slightly from the one calculated by the model, see Fig. 3a, resulting in a shift of the model densification curves to higher temperatures.

The comparison between experiment and model for stainless steel also demonstrates a rapid increase in densification with liquid formation, where full densification is achieved at 10 vol% liquid, see Figs. 3c and 5. The large liquid fraction in GA316L + 0.2B resulted in full densification throughout the range of the experimental sintering temperatures. The model is also able to capture the difference in the sintering

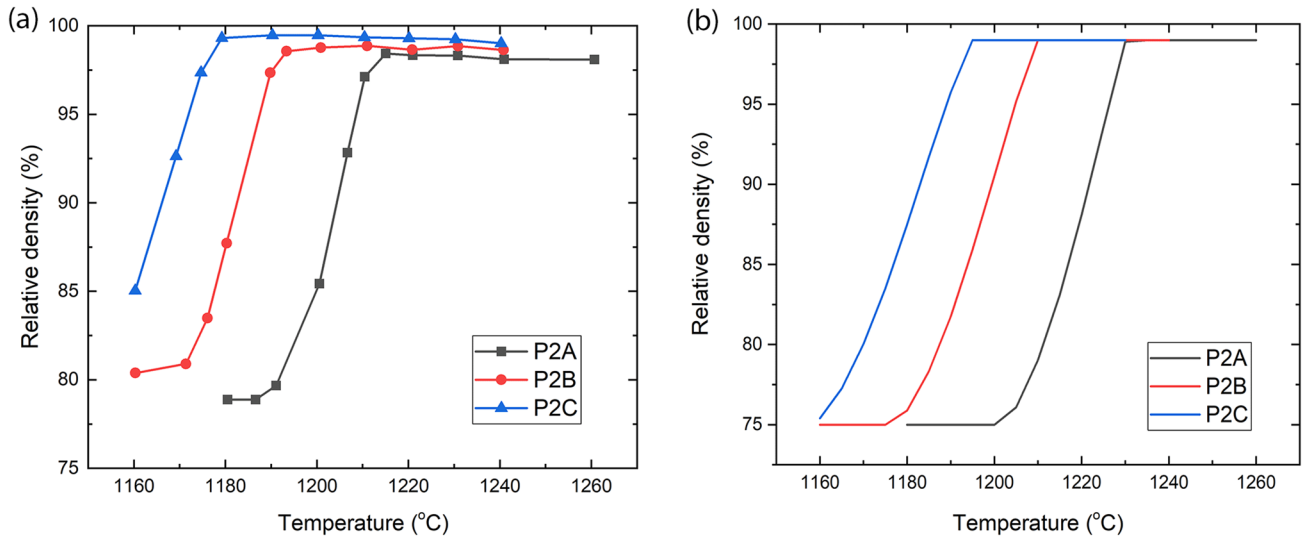

Fig. 4 Comparison of model and experimental measurements for sintered densities as a function of temperature for three tool steels **a** experiment [20] and **b** model

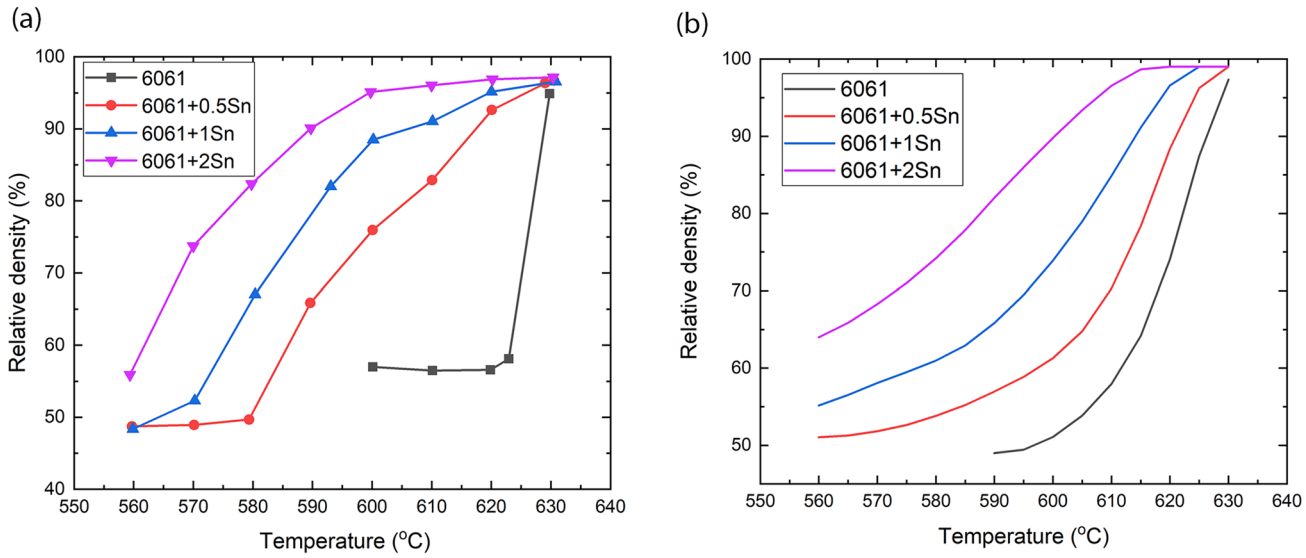

Fig. 6 Comparison of model and measurements of sintered densities as a function of temperature for AA6061 + xSn **a** experiment for sintering in argon [22], error bars not included and **b** model

behaviors between GA316L + 0.8B and WA316L + 0.8B, predominantly due to the difference in the composition of the pre-alloyed powders.

Similarly, it has been demonstrated that the addition of Sn to aluminum alloys reduces the solidus temperature [22, 23], which resulted in a rapid increase in the densification trajectory with temperature. Once again, the model predictions are able to replicate the experimentally observed sintered densities after the addition of elemental Sn to 6061, as shown in Fig. 6.

In general, the observed differences between the measurements and models can be attributed to the following limitations in the model:

1. As shown by the comparison between Fig. 3a and b, the model predicted a rapid increase in densification at higher temperature than the measurements. This is mainly due to the difference in the calculated and measured solidus temperatures. For instance, the solidus temperature for P2A is calculated using CalPhaD to be 1201 °C, which is higher than the measured value (1190 °C) reported by Wright et al.[25].
2. The model in the current study assumes the powder compact has homogenously distributed spherical powders with particle and grain sizes based on the mean values. However, the experimental measurements include distributions of powders sizes with a mix of spherical and non-spherical particles. This will cause a difference in densification across the sample.
3. The modeling in this study also assumes a homogeneous distribution of the liquid phase in the microstructure above the solidus temperature. However, the liquid phase may be inhomogeneously distributed, particularly if there is evaporation from the surface of the sample causing a concentration gradient [28].

Another reason for the deviation between the model and the experimental data, particularly for high-speed steels, is that the experimentally observed grain growth may be suppressed due to secondary phases at the sintering temperature. Note that grain growth in the current model refers to grains of the primary (matrix) phase. The suppression effect by secondary phases in HSS (e.g., MC and/or M6C carbides) on the grains of the matrix phase during SLPS is assumed to be negligible. In general, this assumption is valid at high temperatures where the matrix grains can grow because the grain boundary liquid is dispersed between them. However, at lower sintering temperatures, insufficient liquid limits grain boundary coverage, which will suppress grain growth causing rapid densification.

Validation of Shape Loss

Control of the sintering process may also require knowledge of the macroscopic shape evolution (particularly of shape loss) of the sample. This can be achieved by models that can estimate shape loss in sintering bodies as a function of processing parameters like temperature or geometrical parameters like the initial size and shape of the sample.

Momeni et al. [23] reported shape losses in cylindrical samples after SLPS in two Al-alloys. They characterized shape loss by measuring the ratio of maximum and

minimum diameters, dist = D_{max}/D_{min} of their cylindrical samples after sintering at various temperatures. For the purpose of validation, the model developed in this study is used to estimate the shape loss in terms of their definition by considering the diameters at the bottom and top of the sample, respectively. The simulation is performed considering the processing parameters including the initial size of the sample reported by Momeni et al. [23]. Figure 7 shows comparison of the experimental measurements and model predictions of shape distortion as a function of sintering temperature.

The model results agree well with the experimental data particularly at high temperatures. The experimental data shows a change in the slope of the distortion curve after 610 °C, which is also shown by the model predictions. In addition, the simulation is also able to show the slight difference in shape losses between the two alloys. However, the model's prediction at lower temperatures deviates slightly from the experimental data showing factors other than gravity may contribute to shape loss.

An assumption in the model is that the chemical concentration, particle size distribution and green density is uniform throughout the sample. In this scenario, the maximum diameter (minimum shrinkage) occurs at the bottom of the sample. However, this may not be the case in actual experiments, particularly if there are green density gradients [29] or concentration gradients [28]. Friction between the sample and furnace surfaces may also affect the shrinkage rate at the bottom of the sample and hence the maximum diameter. However, despite the simplifications and assumptions considered in the development of the current model, the observed agreement between the predictions and measurements demonstrates the capability of the model, making it useful for optimizing process parameters for defect free manufacture of components from pre-alloyed powders.

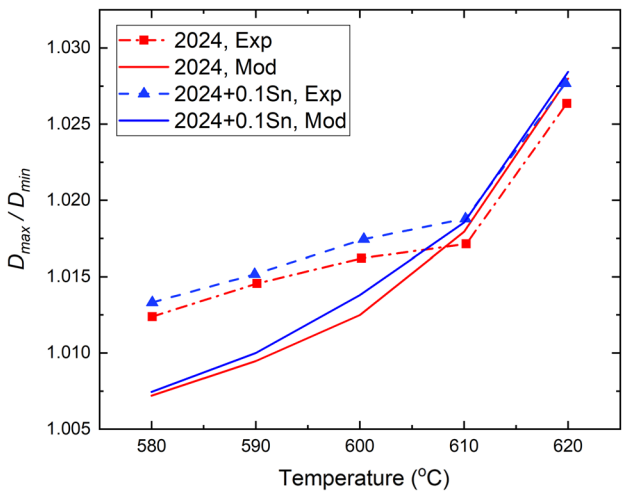

Fig. 7 Comparison of model and experimental measurements for shape distortion in Al alloys

Processing Window for Defect Free Sintering

This section involves development of a microstructural parameter that can be used to optimize the processing window of samples during SLPS. This is performed by keeping the balance of the semi-solid microstructure of the powder compact soft enough to allow densification by viscous flow and strong enough to avoid shape loss through sufficient structural connectivity. This balance is controlled by the volume fraction of liquid, which affects the viscosity of the overall structure through the mean liquid film thickness. However, the mean liquid film thickness at a particular grain size is also affected by the fractional grain boundary coverage by the liquid. Thus, by rearranging Eq. (14), the ratio of the mean liquid film thickness, δ_L and grain size, d at a given temperature can be considered to show the rate of change in microstructural softening of the powder compact, $\dot{\xi}$ during the sintering cycle as:

$$\dot{\xi} = \frac{\delta_L}{d} = \frac{f_l}{3F_c(1-f_l)} \tag{17}$$

During sintering at a constant temperature, coarsening or grain growth (which is proportional to the sintering time) causes an increase in the mean liquid film thickness resulting in a reduction in the viscosity and hence an increase in the likelihood of shape loss. Therefore, the microstructural softening after sintering for time t can be given by integrating Eq. (17) as:

$$\xi = \left(\delta_L/d\right)t \tag{18}$$

By using the model discussed in "Model for densification and shape" section together with Eq. (18), it is possible to estimate the maximum and minimum bounds of softening that are necessary to keep the microstructure of a sintering body (i) strong enough to maintain shape and (ii) soft enough for densification by viscous flow. The two bounds are determined by calculating the mean liquid film thickness corresponding to a defined maximum distortion threshold value and the on-set of densification by viscous flow, as described below.

To find the maximum bound of softening, a shape distortion strain measure, ε_{dist} is first defined by considering the diameters at the top, D_{top} and bottom, D_{bot} of a cylindrical sample as:

$$\varepsilon_{dist} = 100\left(\frac{D_{bot}-D_{top}}{D_{top}}\right) \tag{19}$$

A maximum threshold value for tolerable amount of distortion strain of a given sample can be set, for example,

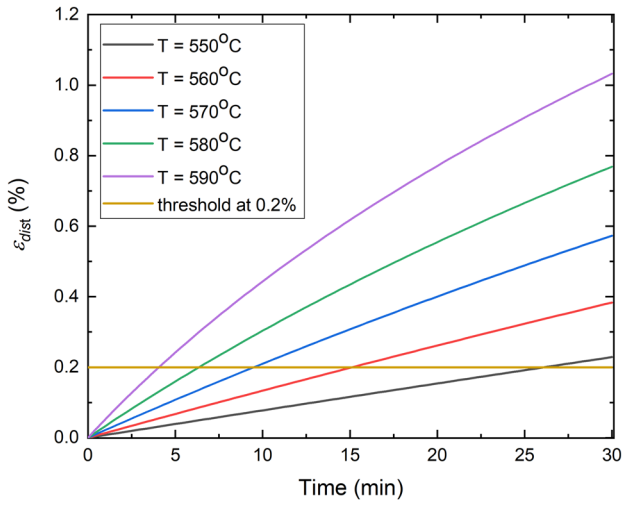

Fig. 8 Distortion of cylindrical sample of Al-2024 as a function of time at different temperatures

at $\epsilon_{\text{dist}} = 0.2\%$. Note that a different threshold value can be considered depending on the user's tolerance level for shape loss. Figure 8 shows an example of model prediction of the distortion strains versus sintering time for Al-2024 after sintering at different temperatures (i.e., between 550 and 590 °C). In addition, Fig. 8 also shows the $\epsilon_{\text{dist}} = 0.2\%$ threshold line demonstrating that the time required to reach the maximum threshold distortion strain decreases rapidly with increasing sintering temperature. This implies that sintering at high temperature will lead to distortion in the first few minutes, giving less time for densification and making it difficult to control shape loss.

The maximum bound of microstructural softening can thus be calculated by extracting the mean liquid film thickness, δ_{L} and instantaneous grain size, d corresponding to the sintering times where the threshold distortion strain line (i.e., $\epsilon_{\text{dist}} = 0.2\%$) crosses the different distortion strain curves, see Fig. 8 together with Eq. (18). This bound of microstructural softening can be considered as the upper limit to maintain shape (avoid significant shape loss).

Similarly, the minimum microstructural softening necessary for densification by viscous flow can be calculated by first considering the local shear stress on grain boundaries. From a rheological perspective, the shear stress on a viscous grain boundary is given by:

$$\tau_{\text{s}} = \frac{\eta_{\text{l}} v_{\text{s}}}{\delta_{\text{L}}} \tag{20}$$

where v_{s} is the viscous sliding rate and η_{l} is the viscosity of the liquid film between grain boundaries. On the other hand, the total shear stress on the grain boundary due to the local capillary stress, $\sigma_{\text{so}} = 4\gamma_{\text{lv}}/d_{\text{p}}$ and weight of the sample can be considered as:

$$\tau_{\text{so}} = \tfrac{2}{3}\left(4\gamma_{\text{lv}}/d_{\text{p}}\right) + \tfrac{2}{3}\rho_b g h \tag{21}$$

To enable grain boundary sliding, the local shear stress given by Eq. (21) should be greater than the shear stress on a viscous grain boundary, i.e., $\tau_{\text{so}} \geq \tau_{\text{s}}$. Thus, the minimum liquid film thickness, $\delta_{\text{L}}^{\text{min}}$ required to drive densification by viscous flow can be determined by combing Eqs. (20) and (21) as:

$$\delta_{\text{L}}^{\text{min}} = \frac{\eta v_{\text{s}}}{\tfrac{2}{3}\left(4\gamma_{\text{lv}}/d_{\text{p}}\right) + \tfrac{2}{3}\rho_b g h} \tag{22}$$

Here, v_{s} can be approximated by using the sintering strain as: $v_{\text{s}} = \dot{\epsilon}/d$. By considering grain growth after sintering at different temperatures (from 550 to 590 °C) and combining Eqs. (18) and (22), the lower bound of microstructural softening necessary for densification can be determined.

Figure 9 shows the minimum and maximum bounds of the microstructural softening, ξ, as a function of sintering temperature. The region between the maximum and minimum bounds can be considered as the window for sintering without significant shape loss. Distortion will occur above the maximum bound, insufficient shrinkage will occur below the lower bound. The sintering window is wider at lower sintering temperatures and narrows with increasing temperature. This demonstrates that the sintering window that allows densification while maintaining shape is very small at high temperatures, making it difficult to control shape.

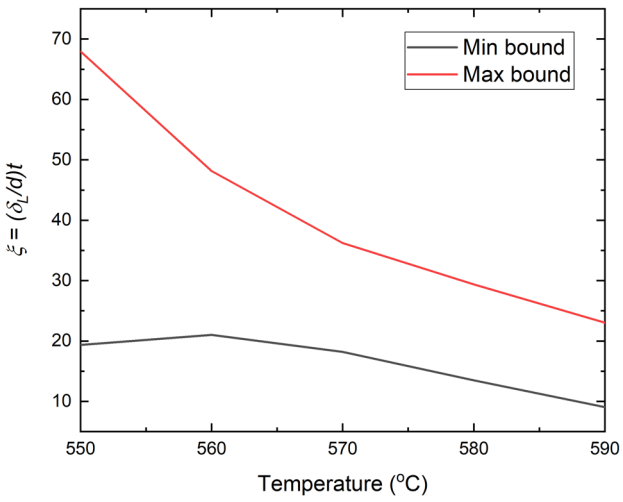

Fig. 9 The minimum and maximum bounds of microstructural softening as function of temperature

Summary

The study presents a computational efficient and predictive model for densification and shape distortion during supersolidus liquid phase sintering (SLSP) of pre-alloyed powder compacts. The model is developed by combining the generalized viscous theory of sintering together with microstructural models for diffusional creep accommodated by viscous grain boundary sliding, enabling the prediction of shrinkage through re-arrangement of particles. Critical thermodynamic and kinetic parameters for the model are obtained from computational thermodynamics, based on the calculation of phase diagrams (CalPhaD) and diffusional transformations (DICTRA) in metals. The predictive capability of the model is presented by comparing simulation results with experimental data from the literature for a variety of engineering alloys. In addition, a processing window for defect free sintering of samples during SLPS is suggested by defining a microstructural softening parameter of a sintering body. The model can be used for computational design of new pre-alloyed powders that are densified by SLPS. In addition, it can also be used to optimize the sintering process for defect free manufacture of components from pre-alloyed powders.

Acknowledgments The author would like to acknowledge Prof Graham Schaffer, from the University of Melbourne, for his valuable feedback and contributions in the preparation of this manuscript.

Funding Open Access funding enabled and organized by CAUL and its Member Institutions.

Declarations

Conflict of interest The author declares that there is no conflict of interest in this work.

References

1. Allen JK, Seepersad C, Choi HJ, Mistree F (2006) Robust design for multiscale and multidisciplinary applications. J Mech Des 128:832–843. https://doi.org/10.1115/1.2202880
2. Choi H, McDowell DL, Allen JK, Rosen D, Mistree F (2008) An inductive design exploration method for robust multiscale materials design. J Mech Des Trans ASME. https://doi.org/10.1115/1.2829860/475435
3. Liu Y, Chen LF, Tang HP, Liu CT, Liu B, Huang BY (2006) Design of powder metallurgy titanium alloys and composites. Mater Sci Eng A 418:25–35. https://doi.org/10.1016/J.MSEA.2005.10.057
4. Deschamps A, Tancret F, Benrabah IE, de Geuser F, van Landeghem HP (2018) Combinatorial approaches for the design of metallic alloys. C R Phys 19:737–754. https://doi.org/10.1016/j.crhy.2018.08.001
5. Molla T, Liu Z, Schaffer GB (2020) Computational efficient modeling of sintering in multi-component alloys for ICME applications. Metall Mater Trans B. https://doi.org/10.1007/s11663-019-01755-1
6. German RM (1997) Supersolidus liquid-phase sintering of pre-alloyed powders. Metall Mater Trans A 28:1553–1567. https://doi.org/10.1007/s11661-997-0217-0
7. Liu J, Lal A, German RM (1999) Densification and shape retention in supersolidus liquid phase sintering. Acta Mater 47:4615–4626. https://doi.org/10.1016/S1359-6454(99)00320-1
8. German RM (2003) An update on the theory of supersolidus liquid phase sintering. In: Proceedings sintering. http://www.cavs.msstate.edu/publications/docs/2003/07/2003-15.pdf. Accessed 4 Sept 2019
9. Liu Y, Tandon R, German RM (1995) Modeling of supersolidus liquid phase sintering: II. Densification. Metall Mater Trans A 26:2423–2430. https://doi.org/10.1007/BF02671256
10. Liu Y, Tandon R, German RM (1995) Modeling of supersolidus liquid phase sintering: I. Capillary force. Metall Mater Trans A 26(9):2415–2422. https://doi.org/10.1007/BF02671255
11. Blaine DC, Bollina R, Park SJ, German RM (2005) Critical use of video-imaging to rationalize computer sintering simulation models. Comput Ind 56:867–875. https://doi.org/10.1016/J.COMPIND.2005.05.013
12. Lai A, German RM (2001) The role of viscosity during supersolidus liquid phase sintering. Met Powder Rep 56:37. https://doi.org/10.1016/s0026-0657(01)80570-1
13. Frandsen HL, Olevsky E, Molla TT, Esposito V, Bjørk R, Pryds N (2013) Modeling sintering of multilayers under influence of gravity. J Am Ceram Soc 96:80–89. https://doi.org/10.1111/jace.12070
14. Olevsky E, Molinari A (2000) Instability of sintering of porous bodies. Int J Plast 16:1–37. https://doi.org/10.1016/S0749-6419(99)00032-7
15. Olevsky EA (1998) Theory of sintering: from discrete to continuum. Mater Sci Eng R Rep 23:41–100
16. Flemings MC (1991) Behavior of metal alloys in the semisolid state. Metall Trans A 22(5):957–981. https://doi.org/10.1007/BF02661090
17. Rahaman MN (2008) Sintering of ceramics. Taylor and Francis Group, Boca Raton, pp 33487–42742
18. Molla TT, Frandsen HL, Bjørk R, Ni DW, Olevsky E (2013) Modeling kinetics of distortion in porous bi-layered structures. J Eur Ceram Soc 33:1297–1305
19. Kim B-N, Hiraga K, Morita K (2005) Viscous grain-boundary sliding and grain rotation accommodated by grain-boundary diffusion. Acta Mater 53:1791–1798. https://doi.org/10.1016/J.ACTAMAT.2004.12.028
20. Wright CS, Youseffi M, Wronski AS, Ansara I, Durand-Charre M, Mascarenhas J, Oliveira MM, Lemoisson F, Bienvenu Y (1999) Supersolidus liquid phase sintering of high speed steels: part 3: computer aided design of sinterable alloys. Powder Metall 42:131–146. https://doi.org/10.1179/003258999665486

21. Bollina R (2005) In situ evaluation of supersolidus liquid phase sintering phenomena of stainless steel 316L: densification and distortion. Pennsylvania State University, State College
22. Liu ZY, Sercombe TB, Schaffer GB (2013) Metal injection moulding of aluminium alloy 6061 with tin. Powder Metall 51:78–83. https://doi.org/10.1179/174329008X284859
23. Momeni H, Shabestari S, Razavi SH (2020) Densification and shape distortion of the Al–Cu–Mg pre-alloyed powder compact in supersolidus liquid phase sintering process. Iran J Mater Sci Eng 17:87–92. https://doi.org/10.22068/IJMSE.17.4.87
24. Molla TT, Ni DW, Bulatova R, Bjørk R, Bahl C, Pryds N, Frandsen HL (2014) Finite element modeling of camber evolution during sintering of bilayer structures. J Am Ceram Soc 97:2965–2972. https://doi.org/10.1111/jace.13025
25. Mezey LZ, Giber J (1982) The surface free energies of solid chemical elements: calculation from internal free enthalpies of atomization. Jpn J Appl Phys 21:1569–1571. https://doi.org/10.1143/JJAP.21.1569/XML
26. Bollina R, Park SJ, German RM (2013) Master sintering curve concepts applied to full-density supersolidus liquid phase sintering of 316L stainless steel powder. Powder Metall 53:20–26. https://doi.org/10.1179/174329009X409688
27. Nandwana P, Kannan R, Siddel D (2020) Microstructure evolution during binder jet additive manufacturing of H13 tool steel. Addit Manuf 36:101534. https://doi.org/10.1016/J.ADDMA.2020.101534
28. Mousapour M, Azadbeh M, Mohammadzadeh A, Danninger H (2020) On the deflection behaviour of prealloyed alpha brass during sintering: in-situ bending technique and modelling. Powder Metall 63:134–141. https://doi.org/10.1080/00325899.2020.1731122
29. Schaffer GB, Huo SH (2000) Distortion in a sintered 7000 series aluminum alloy. Powder Metall. https://doi.org/10.1179/003258900665934